

STATISTICS OF GIANT ARCS IN GALAXY CLUSTERS

NEAL DALAL¹ AND GILBERT HOLDER

Institute for Advanced Study, Einstein Drive, Princeton NJ 08540

JOSEPH F. HENNAWI

Department of Astrophysical Sciences, Princeton University, Ivy Lane, Princeton NJ 08544

Draft version February 2, 2008

ABSTRACT

We study the expected properties and statistics of giant arcs produced by galaxy clusters in a Λ CDM universe and investigate how the characteristics of CDM clusters determine the properties of the arcs they generate. Due to the triaxiality and substructure of CDM halos, the giant arc cross section for individual clusters varies by more than an order of magnitude as a function of viewing angle. In addition, the shallow density cusps and triaxiality of CDM clusters cause systematic alignments of giant arcs which should be testable with larger samples from forthcoming lensing surveys. We compute the predicted statistics of giant arcs for the Λ CDM model and compare to results from previous surveys. The predicted arc statistics are in excellent agreement with the numbers of giant arcs observed around low redshift ($0.2 \lesssim z \lesssim 0.6$) clusters from the EMSS sample, however there are hints of a possible excess of arcs observed around high redshift $z \gtrsim 0.6$ clusters. This excess, if real, appears to be due to the presence of highly massive or concentrated clusters at high redshifts.

Subject headings: gravitational lensing — galaxies: clusters — dark matter

1. INTRODUCTION

Clusters of galaxies provide some of the most spectacular examples of gravitational lensing. The popular images of Abell 2218 and CL0024+1654 that are prominent on the Hubble Space Telescope public website (www.hubblesite.org) show very elongated multiply imaged background galaxies whose features have been distorted by the deep gravitational potential of the galaxy cluster. Such cluster lenses have a variety of cosmological uses. For example, these natural gravitational telescopes can greatly magnify distant sources, allowing us to study the properties of otherwise unobservable galaxies (e.g. Blain et al. 1999; Metcalfe et al. 2003; Smail et al. 2002). In addition, strongly lensed arcs offer a unique, direct probe of the cluster gravitational potential on scales where dark matter is expected to be the dominant component. Heating, cooling, and star formation can have a significant impact on baryons but the dark matter, and therefore the total potential, should be relatively unaffected by these poorly understood processes. Lastly, the incidence of giant arcs may be used to study the background cosmology itself. Bartelmann et al. (1998, hereafter B98) found that the predicted number of giant arcs varies by orders of magnitude among different cosmological models. In light of mounting evidence supporting the Λ CDM model (e.g. Spergel et al. 2003), the spectacular images of giant arcs have led to an embarrassment of riches, as B98 found that the observed instances of giant arcs exceeded their predicted rate by an order of magnitude.

The original discrepancy reported in B98 was based on a subsample of 16 of the most massive clusters (Le Fevre et al. 1994) in the EMSS survey and the arc frequency (roughly 20% of very massive clusters) was

confirmed in the larger EMSS sample of Luppino et al. (1999). A subsequent survey based on optically-selected clusters in the Las Campanas Distant Cluster Survey (Zaritsky & Gonzalez 2003) found comparable giant arc frequencies, while a recent report by the Red Cluster Sequence cluster survey group (Gladders et al. 2003, 2002) found a high probability ($\sim 30\%$) of a lensing cluster showing more than one source being distorted into a giant arc.

On the theoretical side, significant work has gone into refining the expected number of giant arcs. Several works have confirmed the lensing cross-sections of B98 (Bartelmann et al. 2003; Meneghetti et al. 2003b, 2001), but other recent work has suggested that the cross-sections of B98 may be too low. In particular Wambsganss et al. (2003) used numerical simulations and found that the cross-section was a very steep function of redshift and that the anomalous cross-sections could be brought into agreement by allowing a broader range of source redshifts. Oguri et al. (2003) used analytic models with triaxiality and found that allowing a steeper central density profile enhanced the lensing cross-section to a level that was close to the observed lensing frequency of the EMSS sample.

In this paper we go back to the beginning of the problem (i.e., B98) to repeat the analysis on a larger sample of simulated clusters and update the statistics for the EMSS lensing sample. We then apply the analysis to recent optical catalogs to determine the extent, if any, of the discrepancy between observations and theory. Lastly, we investigate what new information may be gleaned from upcoming deep, large area surveys like the CFHT Legacy survey, which should produce large numbers of new strongly lensed arcs.

¹ Hubble Fellow

2. CLUSTER LENSING SIMULATIONS

We estimate giant arc statistics by ray-tracing through cosmological N-body simulations. Below, details of the calculation are briefly described.

2.1. N-body simulations

We used the publicly available simulation outputs of the Virgo Project². We used the Λ CDM simulations that were performed as part of the GIF project (Kauffmann et al. 1999). The cosmological parameters were $\Omega_m = 0.3$, $\Omega_\Lambda = 0.7$, $h = 0.7$, power spectrum shape parameter $\Gamma = 0.21$, and mass power spectrum normalization $\sigma_8 = 0.9$. The comoving simulation box length was $141.3 h^{-1}$ Mpc and 256^3 particles were used, leading to a mass per particle of $10^{10} h^{-1} M_\odot$. The gravitational softening length was $20 h^{-1}$ kpc. Simulation outputs were available at a variety of redshifts, allowing accurate allowance of time evolution in cluster properties. A subset of the clusters from these simulations were used as part of the ensemble of simulated clusters used in B98.

2.2. Lensing calculation

To compute giant arc statistics for the N-body simulations described above, we adopt a technique similar to that pioneered by Bartelmann & Weiss (1994) and employed by subsequent workers (e.g. Bartelmann et al. 1998; Meneghetti et al. 2003a, 2000, 2001). We first project the dark matter density onto a two dimensional regular grid. Typically we used a 256×256 grid covering a square $4h^{-1}$ comoving Mpc on a side, centered on the cluster. From the projected surface density Σ , the convergence for each lens and source redshift pair is given by $\kappa = \Sigma / \Sigma_{\text{crit}}(z_l, z_s)$, where Σ_{crit} is the critical surface density for strong lensing (Schneider et al. 1992). Then, the deflection angle map $\alpha(\mathbf{x})$ is constructed (via Fourier transform) on the same grid. Given this map, we then ray trace a finer 4000×4000 grid covering a subset of the image plane onto the source plane, linearly interpolating the deflection between the grid points of the coarser 256^2 grid. We set up a regular grid on the source plane; each source plane pixel contains a linked list of all image plane pixels which ray trace to the source plane pixel. Having performed this single ray trace, it is then a simple matter to construct the lensed arcs for an arbitrary source by concatenating the lists for all source plane pixels falling in the source. We emphasize that the use of linked lists greatly speeds the calculation – only one single ray trace is performed, after which arcs may be constructed for many different source positions, sizes and geometries for essentially no computational cost.

For each source, the pixel lists are then sorted into separate arcs, by grouping together neighboring pixels. We measure arc properties using methods based on Bartelmann & Weiss (1994). The arc area and magnification are found by summing the areas of the pixels falling in the arc. Arc lengths are estimated by first finding the arc centers, then finding the arc pixel furthest from the centroid, as well as the pixel furthest from this pixel. As in B98, the arc length was then given by the sum of the lengths of the two line segments connecting these three points. The arc width was defined as the ratio of the arc area to the arc length. See figure 1 for an example.

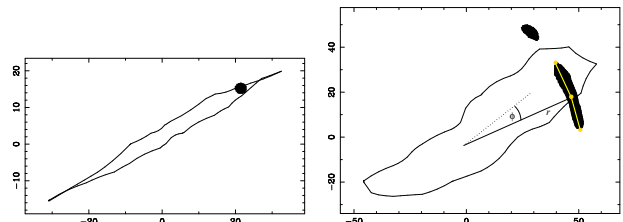


FIG. 1.— Example of simulated arcs. The source plane (left) and image plane (right) are illustrated. Solid lines depict the approximate locations of the critical lines and caustics, while filled regions show the pixels falling inside the source (left panel) and the corresponding lensed images (right panel). Two arcs are found for this source, with length to width ratios of 7.5 and 2.8 respectively. For the long arc, the arc radius r and position angle ϕ (relative to the major axis of the mass distribution) are labeled.

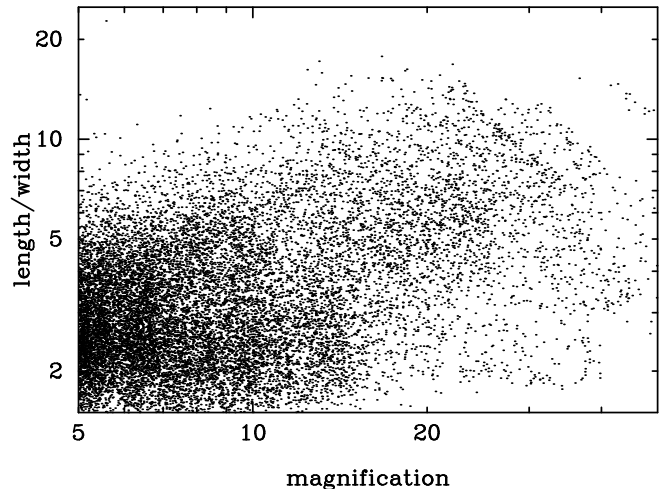


FIG. 2.— Magnification vs. length/width ratio. While these two quantities are equal for isothermal lenses, giant arcs tend to form at small radii ($r < r_s$) where the density profile is shallower than isothermal. Here we plot all arcs in one cluster projection with magnification $\mu > 5$, however only $\sim 40\%$ of the points have length/width ratios $r > 5$.

The relation between length/width ratio and magnification is sensitive to the slope of the halo potential (Williams & Lewis 1998) and can also be affected by local perturbations in the projected mass distribution. In figure 2 we plot arc magnification against length/width ratio using the above method. We find good agreement with the mean trend of length/width vs. magnification with the predictions of Williams & Lewis (1998) for typical clusters in the simulations. However, there is substantial scatter in this relation that is likely caused by random source orientations and local fluctuations in the surface mass density. It is apparent that highly distorted images will also be highly magnified, but the converse is not true.

For each cluster projection, we compute giant arc statistics using a Monte Carlo approach. We randomly place elliptical sources, with axis ratios drawn uniformly in the range $q \in [0.5, 1]$ and random position angles. We count as giant arcs only those images with length/width ratios $r \geq 10$, making no distinction between radial and tangential arcs, although we note that the latter dominate the cross section. Cross sections are then computed by multiplying the fraction of sources producing

² <http://www.mpa-garching.mpg.de/Virgo>

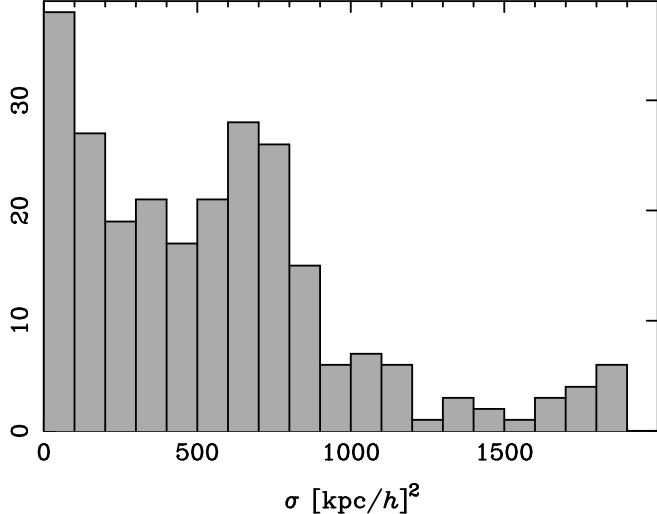


FIG. 3.— Histogram of cross-sections for the 4th most massive cluster at $z = 0.2$ under different projections.

giant arcs in the Monte Carlo by the area over which the sources were randomly distributed.

2.3. Cross sections

The giant arc cross section for a single cluster varies enormously as a function of orientation, as shown in fig. 3. A factor of ~ 20 spread in σ is not uncommon. Additionally, the distribution is quite skewed, with a tail extending to high σ . This appears to be due to the large degree of substructure and ellipticity/triaxiality in the density profiles. Orientations with large cross sections are typically those which project along the cluster major axis, or which project massive substructures onto small radii. Unfortunately, this means that shot noise will be persistent in any calculation of arc statistics; large numbers of projections are required for trustworthy mean cross sections. In the calculations below, we compute mean cross sections by averaging over 251 orientations for each of the top 20 most massive clusters at each redshift, while we perform 3 projections each for the next 100 clusters.

In addition to the scatter in cross section for individual clusters, there is large scatter among cross sections of clusters of similar mass, shown in Figure 4. The error bar for each cluster shows the error in the mean, averaged over all orientations. The dispersion for each cluster is comparable to the mean. The mean lensing cross-section as a function of mass shows a dramatic rise at a mass of a few $10^{14} h^{-1} M_{\odot}$ and an apparent flattening at the highest masses; the numbers become too low to say anything definite at high masses, as shown by the large error bar in the highest mass bin.

When weighted by the number of clusters at each mass (right panel) there is an apparent peak at $\sim 7 \times 10^{14} h^{-1} M_{\odot}$. The significance of this peak is hard to judge; given the low numbers of clusters in the highest mass bin, and the large scatter among cross sections in each bin, we cannot definitively say whether we are underestimating the total optical depth by neglecting massive clusters too rare to appear in our limited simulation volume. On the other hand, the peak corresponds ex-

actly to the mass range expected of massive X-ray luminous galaxy clusters which appear to dominate the giant arc optical depth observed by surveys like EMSS. In addition, we know that the rise of $\langle \sigma \rangle$ with m must flatten at high masses, once the Einstein radii approach the NFW scale radius r_s . This ensures that, at some high mass, the exponentially declining mass function $n(m)$ will overpower the growing $\langle \sigma \rangle(m)$. We will assume that our simulation volume provides a fair sample of the objects causing most of the lensing, with the caveat that our estimates might plausibly be low by a factor of ~ 2 .

A related caveat is that, since the total optical depth is dominated by the most massive clusters, great caution must be employed before deriving cosmological constraints from giant arc statistics. While the abundance of such clusters depends in part on cosmological parameters like Ω_{Λ} , it also depends sensitively upon the matter power spectrum (e.g. Bahcall & Fan 1998; Haiman et al. 2001). Strong prior constraints on parameters like σ_8 must be applied (and believed) before constraints can be derived on parameters like Ω_{Λ} or w .

2.4. Arc properties and cluster galaxies

The effects of cluster galaxies on the formation of giant arcs have been investigated by Meneghetti et al. (2000) and Flores et al. (2000), and the effects of central cD galaxies in particular were studied by Meneghetti et al. (2003a). These authors found that cluster galaxies are generally unimportant, except for central cD galaxies which can enhance the giant arc cross section by $\sim 50\%$.

The relatively small effect of cluster galaxies on the arc formation cross section is not surprising. Giant arcs typically form at large radii relative to the cluster center, $\sim 20 - 30''$; see figure 5. A mass $m \approx \Sigma_{\text{crit}} \cdot \pi r^2 \approx 10^{14} h^{-1} M_{\odot}$ is interior to these arcs, much larger than the typical masses even of cD galaxies, $\lesssim 10^{13} M_{\odot}$. Accordingly, we do not expect the cross sections for formation of these wide separation arcs to be grossly affected by the presence or absence of galaxies in the simulations. On the other hand, galaxies can strongly affect the cross section for formation of smaller separation arcs. To illustrate, we plot in figure 6 the distribution of arc radii produced by clusters from the $z = 0.3$ output, lensing sources at $z_s = 2$. We artificially added mass concentrations to the cluster centers in two ways: as point masses of varying mass, and as galaxies with fixed velocity dispersion (350 km/s) and varying mass. It is apparent from the figure that mass is a less important determinant of arc properties than central mass concentration, here parameterized by velocity dispersion. Galaxies of different masses (e.g. 3×10^{12} and $10^{13} h^{-1} M_{\odot}$) but the same velocity dispersion produce nearly indistinguishable effects on the radial distribution. Increasing the central mass concentration can greatly increase the number of giant arcs forming at small radii, illustrated by the curves for which point masses were added to the central pixel. However, it would appear that arc statistics at very large radii ($\gtrsim 20''$) are unaffected by these central mass concentrations. Even at moderate radii ($\gtrsim 10''$), the difference between the statistics for pure dark matter simulations and those including reasonably sized galaxies is not dramatic.

Accordingly, we expect that our pure dark matter simulations should provide a reasonably accurate estimate

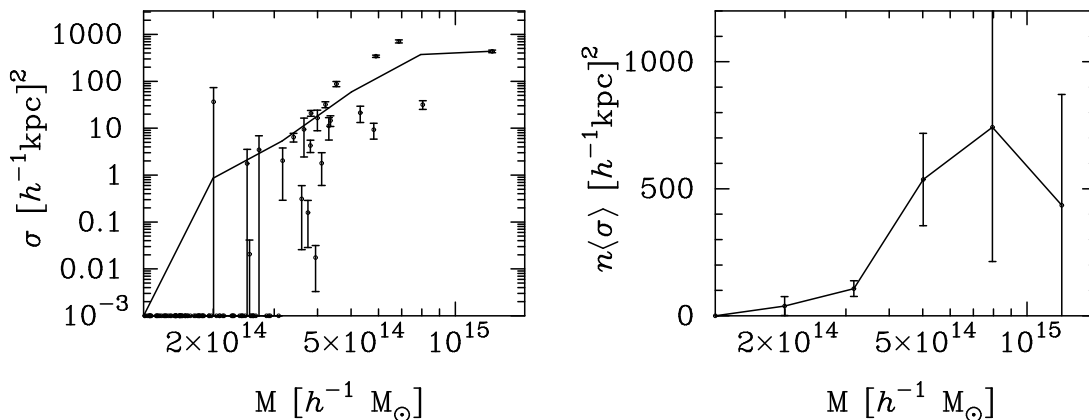


FIG. 4.— Cross-section for forming giant arcs (left) and cross-section weighted by number of clusters (right) for simulation volume at $z_l = 0.2$ and a source redshift $z_s = 1$. Cross sections are given in physical distances on the source plane. The solid line in the left panel is the mean cross section $\langle\sigma\rangle$ averaged over bins of width 0.2 in $\log_{10} M$. Error bars in the left panel show error in the mean cross-section per cluster, not the dispersion, while the error bars in the right panel include the effect of Poisson statistics.

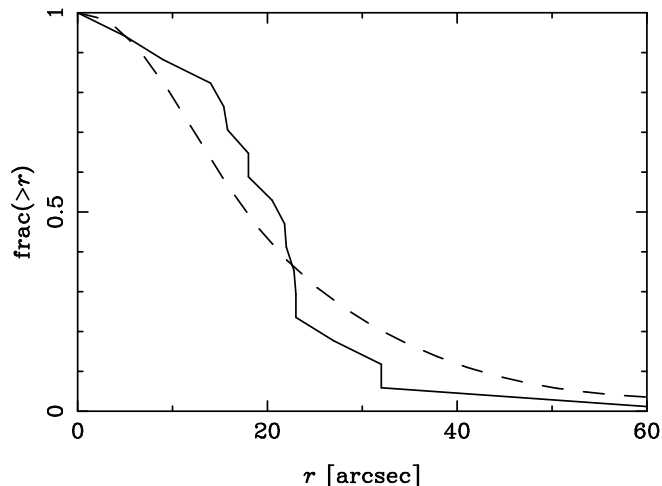


FIG. 5.— Radial distribution of giant arcs, as measured by Luppino et al. (1999) (solid line), and as predicted by the $z = 0.3$ GIF clusters (dashed line).

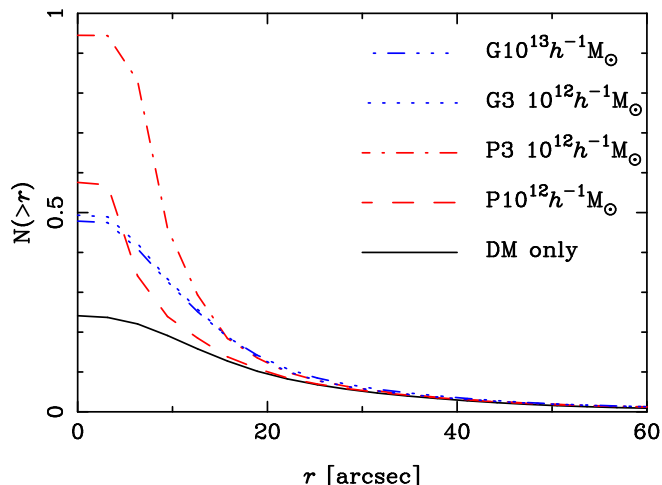


FIG. 6.— Number of $z_s = 2$ giant arcs produced by a $(141 h^{-1} \text{Mpc})^3$ volume of clusters at $z = 0.3$. The solid line shows results from the dark matter distribution alone, the ‘P’ curves show results when a central point mass is added, and the ‘G’ curves show the effects of adding a central singular isothermal sphere with velocity dispersion $\sigma = 350 \text{ km/s}$.

for the optical depth for wide separation giant arcs in the Λ CDM model. However, absent a prescription for galaxy formation, we cannot make reliable predictions for the numbers of intermediate separation ($r \lesssim 5''$) arcs, which will prove to be a limitation in the interpretation of high redshift giant arc surveys.

Although cD galaxies do not dramatically change the wide separation arc cross section, they can have important effects on giant arc properties. For example, Williams et al. (1999) have argued that massive ($M \sim 3 \times 10^{12} M_\odot$) galaxies are required at the centers of most low redshift arc-bearing clusters in order to explain observed arc widths. Central galaxies also affect the angular distribution of long, thin arcs about the cluster center. As an example, we plot in figure 7 the angular distribution of giant arcs about one particular cluster, as a function of the mass of the central cD galaxy painted onto the surface density. In the top panel, corresponding to pure DM with no added galaxy, the giant arcs tend to form only at the ends of the critical line. As the mass becomes more centrally concentrated, the critical lines do not change dramatically in size, however giant arcs begin to form all around the critical lines, instead of only along the cluster major axis.

This is shown more quantitatively in figure 8, which plots the angular distribution of arcs about the cluster center, relative to the cluster major axis. About 80% of giant arcs form at position angles within 45° of the cluster major axis in the pure DM simulations. The large anisotropy in the angular distribution is diminished somewhat by the addition of the central galaxy; nevertheless we expect a residual anisotropy to be present for realistic galaxy masses. For example, adding a central mass of $3 \times 10^{12} h^{-1} M_\odot$ decreases the fraction of arcs within 45° of the major axis to $\sim 70\%$. Under the assumption that the cluster major axis can be determined from the brightest central galaxy position angle, this prediction can be tested using clusters even which have only one arc. This anisotropy signal may be washed out by misalignments between the BCG orientation and halo orientation, however for multi-arc clusters the anisotropy should also be manifest in the distribution of relative position angles of arcs, $\phi_{12} = \phi_1 - \phi_2$, also shown in figure 8.

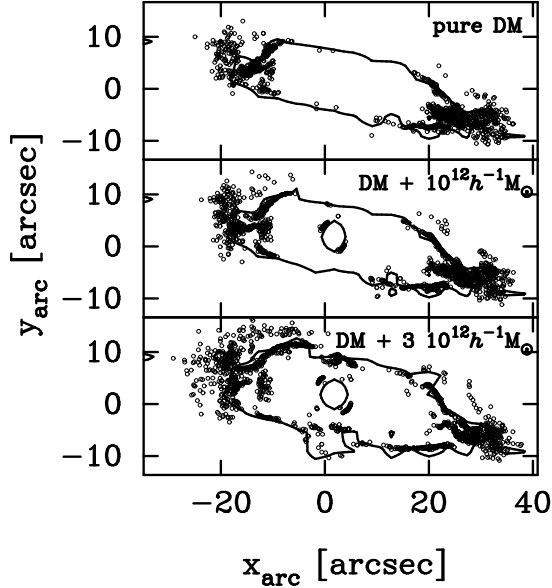


FIG. 7.— Angular distribution of giant arcs for one cluster projection. The panels correspond, from top to bottom, to results from the DM simulation with added central point masses of 0, 1, and $3 \times 10^{12} h^{-1} M_{\odot}$ respectively. The solid lines are the critical curves, and symbols show the centers of giant arcs produced in the Monte Carlo.

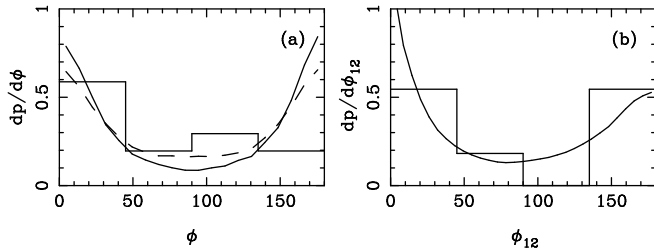


FIG. 8.— Distribution of arc position angles from $z = 0.3$ GIF clusters. The left panel shows arc position angles relative to the major axis of the projected dark matter distribution, for pure DM (solid) and $DM + 3 \times 10^{12} h^{-1} M_{\odot}$ (dashed). The histogram shows the same distribution for the EMSS arcs. The right panel shows the distribution of relative position angles between pairs of arcs in multi-arc systems, $\phi_{12} = \phi_1 - \phi_2$, for DM only. The histogram shows the ϕ_{12} distribution for the three EMSS clusters showing multiple giant arcs.

This behavior can be easily understood, as outlined in more detail in the appendix. The caustic structures of the pure dark matter case often take the form of “lips” catastrophes, while the addition of the central mass transforms these into the more familiar radial and tangential caustics. Lips caustics tend to form giant arcs only at the ends of the critical line, while tangential caustics can form giant arcs at a wide variety of position angles.

Since we have no reliable model for populating CDM halos with galaxies, we cannot at present make predictions regarding the angular distribution of arcs around clusters. However, our crude treatment of central galaxies seems to indicate that typical cD galaxies do not fully isotropize the arc angular distribution. It will therefore be interesting to measure the angular distribution with upcoming wide-angle, deep lensing surveys which should find numerous multi-arc clusters. If clusters have lips,

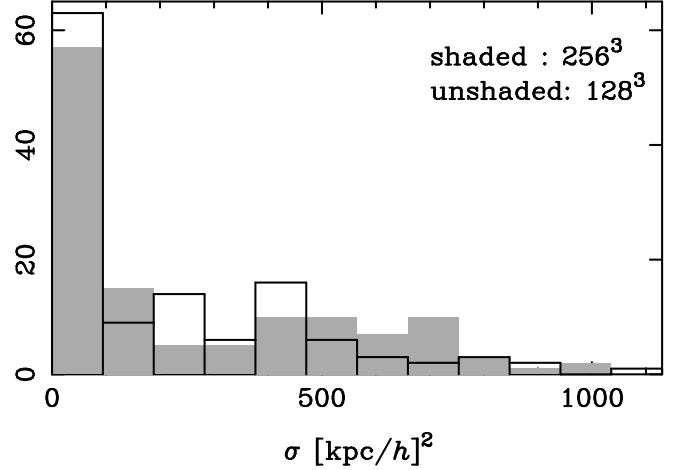


FIG. 9.— Histogram of cross-sections for the same $M = 4 \times 10^{14} h^{-1} M_{\odot}$ cluster at $z = 0.3$ simulated at two different resolutions. The shaded histogram corresponds to the high resolution simulation, with a mean cross section for producing $l/w > 10$ arcs at $d > 10''$ of $\langle \sigma \rangle = 210 (h^{-1} \text{kpc})^2$. The unshaded histogram corresponds to the low resolution simulation, which gives $\langle \sigma \rangle = 250 (h^{-1} \text{kpc})^2$.

then multiple arcs in a cluster should tend to form along the cluster major axis, at the ends of the critical curve.

2.5. Numerical resolution

We argued above that our dissipationless N-body simulations cannot be used to make reliable predictions for arc statistics at small radii, while at large radii ($d > 10 - 20''$), neglect of baryonic physics should not change our results significantly. Even at large radii, however, another possible source of error is particle noise in the simulation. Collapsed objects represented by low numbers of particles will suffer artificially from two-body relaxation effects, which can significantly affect the inner structures of simulated halos. Power et al. (2003) find that halos satisfying $t_{\text{relax}}(r) = t_{\text{dyn}} N(< r) / [8 \log N] > 0.6 H_0^{-1}$ may safely be assumed to be free of relaxation effects. We are interested in measuring arc properties at radii $r \sim 50 - 100 h^{-1} \text{kpc}$ for objects of mass $M \gtrsim 10^{14.5} h^{-1} M_{\odot}$. For such objects, the Power et al. bound implies a minimum of $N(r_{\text{Ein}}) \gtrsim 1500$ particles representing the profile interior to the arc radius, or a particle mass not exceeding $m_p \lesssim 4 \times 10^9 h^{-1} M_{\odot}$. For comparison, the Λ CDM GIF simulations have particle masses of $1.4 \times 10^{10} h^{-1} M_{\odot}$, in excess of this bound. Hence, it is unclear from this simple analysis if our results will be affected by particle noise. Two-body relaxation can also become important if the force softening is insufficient. Power et al. argue that a force softening length $\epsilon \approx 4 r_{\text{vir}} / \sqrt{N_{\text{vir}}}$ is optimal. For our example halo this works out to about $\epsilon_{\text{opt}} \approx 16 h^{-1} \text{kpc}$; while in comparison the GIF Λ CDM simulations use a softening of $20 h^{-1} \text{kpc}$.

To test whether such resolution effects will significantly impact on our conclusions, we perform the following convergence test. We perform two simulations of a $(100 h^{-1} \text{Mpc})^3$ volume at two different resolutions, using the TreePM code³ (kindly made publicly available by P. Bode and J. P. Ostriker). The low resolution simulation

³ see <http://www.astro.princeton.edu/~bode/TPM/index.html>

uses 128^3 particles with mass $m_p = 3.6 \times 10^{10} h^{-1} M_\odot$ and force softening length $\epsilon = 20 h^{-1}$ kpc, while the high resolution simulation has 256^3 particles of mass $m_p = 4.5 \times 10^9 h^{-1} M_\odot$ and softening $\epsilon = 10 h^{-1}$ kpc. To ensure that the same objects would form in both simulations, they were initialized using the same random phases for all modes common to the two boxes, while the higher resolution run contained additional high- k power. We then compared individual clusters from each simulation. One example is shown in Figure 9; the other clusters we checked showed similar levels of agreement between the two resolutions. We therefore conclude that the resolution of the GIF simulations is adequate for our purposes.

3. HOW MANY LUMINOUS GIANT ARCS?

Following the considerations of §2.2.4, we will count in our statistics only those arcs with length-to-width ratios $r \geq 10$, and distances relative to the cluster center of $d \geq 10''$ in order to minimize the uncertainties from the galaxy contribution.

The optical depth for forming an arc can be derived for each simulation volume as a sum over all clusters in the box:

$$\frac{d\tau}{dz_l}(z_s) = \frac{dV_{co}/dz_l}{L_{box}^3} \sum_{j=1}^{N_{clus}} \frac{\bar{\sigma}_j(z_s)}{d_A^2(z_s)} \quad (1)$$

The total optical depth as a function of source redshift $\tau(z_s)$ is then simply a sum over simulation volumes. The number of arcs expected per square degree is then given by

$$N_{arcs} = \int_0^\infty dz_s \tau(z_s) \frac{dN_{source}}{dz_s}, \quad (2)$$

where dN_{source}/dz_s is the source density that could form observable arcs.

In figure 10 we plot the contribution to the giant arc optical depth from different lens redshifts, for three different source redshifts. As Wambsganss et al. (2003) have stressed, the optical depth increases with source galaxy redshift: we find optical depths of 0.25, 0.70, & 1.4×10^{-6} for source redshifts $z_s = 1, 1.5$, and 2 respectively. However, we find that the variation with redshift, while substantial, is not as strong as that reported by Wambsganss et al. (2003).

The source density term is of equal importance to the optical depth term. To estimate the number density of galaxies as a function of redshift and limiting magnitude, we employ the photometric catalogs of Fontana et al. (2000), compiled from galaxy counts from the Hubble Deep Fields. We divided source galaxies into three bins: $0.75 \leq z_s < 1.25$, $1.25 \leq z_s < 1.75$, and $z_s > 1.75$.

Magnification bias may or may not be important. In a strictly flux-limited survey, magnification bias would be important, but there is no magnification bias in the limit where all sources are resolved and surface brightness is the limiting concern. For giant arc surveys, neither regime is appropriate. Arc detection is closer to being limited by surface brightness than by integrated flux, but adaptive smoothing can modify this. The observed source distribution is expressed in terms of integrated flux, but ground-based surveys may be missing

TABLE 1. SURVEY STATISTICS

Survey	redshifts	area	depth	N_{obs}	N_{pred}
EMSS ¹	$0.15 < z \lesssim 0.6$	~ 360	$V < 22$	8	8.2
LCDCS ²	$0.5 < z < 0.7$	69	$R < 21.5$	2	1.2
RCS ³	$z < 0.6$	90	$\mu_R < 24$	0	2
	$z > 0.6$			4	1

Note. — Survey areas are given in square degrees. For the LCDCS, quoted arc statistics are for all radii, with no cut on arc radius, while RCS statistics are for arcs in their primary sample with $d > 10''$. References are: (1) Luppino et al. (1999), (2) Zaritsky & Gonzalez (2003), (3) Gladders et al. (2003).

distant compact sources because seeing can reduce their apparent surface brightness. In what follows we include magnification bias when comparing to catalogs that are nominally magnitude-limited.

3.1. The EMSS Sample

In comparing to observations it is essential that the effective area of the survey is well-known. For the EMSS, calculating the effective survey area is non-trivial. The survey area is a strong function of limiting flux (Henry et al. 1992). For each cluster detected in the EMSS we found the sky area A_i over which that cluster could have been detected. An estimate of the cluster surface density is then given by $\sum 1/A_i$ clusters per square degree. The EMSS lensing sample of Luppino et al. (1999) is defined by clusters with $L_x > 2 \times 10^{44} \text{ erg s}^{-1}$ and $z > 0.15$. Using the Henry et al. (1992) coverage, we find that the surface density of EMSS clusters is one cluster per 9.6 square degrees, a total coverage for the 38 clusters of 360 square degrees. The earlier sub-sample of 16 clusters, used in Le Fevre et al. (1994), is defined by $L_x > 4 \times 10^{44} \text{ erg s}^{-1}$ and $z > 0.2$, for which the surface density is one cluster per 20 square degrees.

Of the 38 most massive EMSS clusters, 8 show giant luminous arcs. Extrapolating over the entire sky we would therefore expect roughly 900 giant arcs. The sub-sample used by Le Fevre et al. (1994) showed 6 clusters with giant arcs, which translates into one arc-inducing cluster every 53 square degrees or roughly 800 giant arcs on the entire sky. The consistency of these two values supports our estimate for the area covered by EMSS.

We can roughly estimate the expected number of arcs by taking the optical depths from figure 10 and multiplying by an appropriate source galaxy density. Assuming that arcs with length/width ratios $r \geq 10$ are magnified by about 2.5 magnitudes, and noting that Le Fevre et al. (1994) counted arcs with integrated magnitudes $V < 22$, we find galaxy densities for $V < 24.5$ of 7.4, 1.4, and 2.6 arcmin^{-2} for our three redshift bins from the Hubble Deep Fields. Multiplying by the corresponding optical depths (0.25, 0.70, & 1.4×10^{-6}) gives a total of ~ 940 arcs expected over the full sky. An alternative estimate for the number of arcs may be obtained not by assuming arcs are magnified by ~ 2.5 magnitudes, but instead convolving the calculated arc magnification distribution with the observed luminosity function. This estimate would be valid in the limit that low surface brightness arcs with total integrated magnitudes brighter than the detection threshold are observable. For a threshold in-

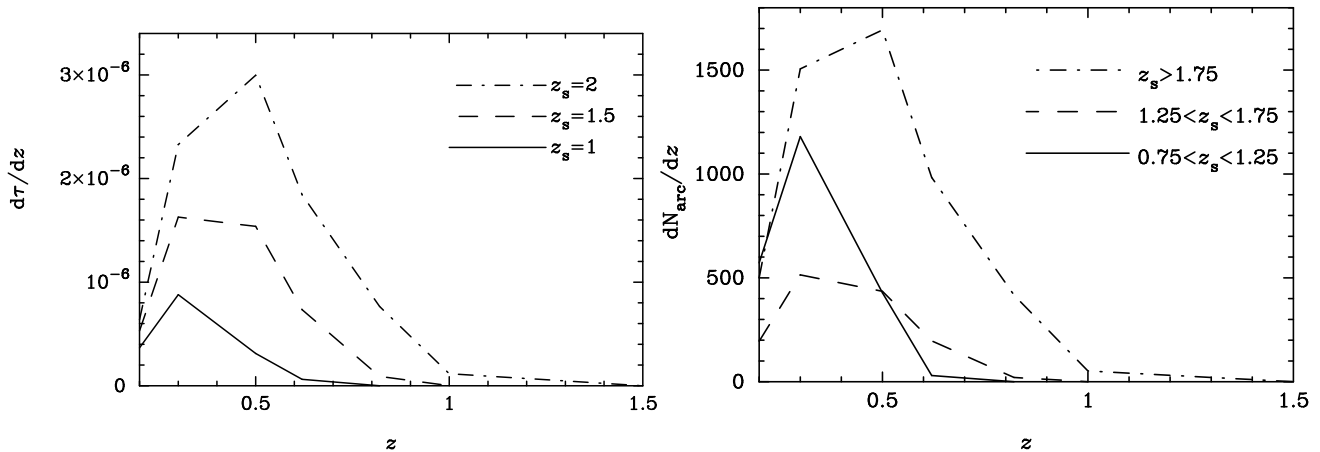


FIG. 10.— The left panel shows the optical depth for arcs with length/width ≥ 10 and distance from cluster center $d > 10''$, as a function of redshift for GIF simulations. The right panel shows the number of arcs with total integrated magnitude $V < 22$ as a function of lens redshift, for three different source redshift bins. The declining number density of sources with increasing redshift somewhat counteracts the increase of optical depth with redshift.

egrated magnitude of $V < 22$, the HDF galaxy counts reported by Fontana et al. (2000) give ~ 1400 giant arcs with $r \geq 10$ located $d \geq 10''$ from the cluster center, over the full sky.

Apparently, there is no excess in the number of giant arcs observed around EMSS clusters compared to expectations from the Λ CDM model. It appears that the solution to what was thought to be an order of magnitude problem is in a conspiracy of small effects: a larger effective area for the EMSS than estimated in B98 (factor of 2), a higher source density (factor of 2), and a somewhat higher redshift-averaged optical depth (factor of 2).

3.2. LCDCS Sample

Zaritsky & Gonzalez (2003) surveyed clusters in the range $0.5 \leq z \leq 0.7$ over a 69 deg^2 field. In this area, they found two giant arcs with $R < 21.5$ and length $L > 10''$, and a number of additional arcs and arc candidates with which they do not include in their statistics. A straightforward comparison with our expected statistics is complicated by the fact that both of these arcs are located close ($\lesssim 10''$) to cluster galaxies. As mentioned in §2.2.4, the optical depth for such close-in arcs is strongly affected by the presence of galaxies which are neglected in the pure dark matter simulations we have used.

Nevertheless, we can try to make some rough estimates for the expected giant arc rate. Dropping the $d > 10''$ cut we imposed for the EMSS sample, we find that over the range $0.5 < z < 0.7$, the GIF clusters produce 0.7 arcs in the 69 deg^2 surveyed in the LCDCS. If we paint galaxies with $\sigma = 350 \text{ km/s}$ and $M = 3 \times 10^{12} h^{-1} M_\odot$ onto the clusters, the expected number increases to 1.2 giant arcs.

Accordingly, it appears that the giant arc incidence measured by the LCDCS is consistent with predictions from the Λ CDM model. However, Zaritsky & Gonzalez emphasize that their measured giant arc statistics should be viewed as a lower bound on the true incidence; a less conservative cut on arcs in their sample could lead to a statistically significant discrepancy. On the other hand, Zaritsky & Gonzalez also note that their estimated clus-

ter number density is $4.5\times$ higher than that of the EMSS at these redshifts, which could artificially enhance the LCDCS arc rate relative to the full sky average.

3.3. RCS Sample

Gladders et al. (2003) survey 90 deg^2 for giant arcs, counting only arcs with surface brightness in R_C of $\mu_R < 24 \text{ mag arcsec}^{-2}$. In their primary sample, Gladders et al. detect a total of 5 arc candidates, four of which have length-to-width ratios $r \geq 10$. Oddly, all five of the arc-candidate clusters in their primary sample have high redshifts, $z \geq 0.64$. From the EMSS statistics, we would expect on average ~ 2 arc-producing clusters in the range $0.15 \leq z \leq 0.6$ over a 90 deg^2 field, so the lack of such clusters in the RCS sample is unusual but not significantly discrepant.

Since Gladders et al. impose a surface brightness cut on their arc candidates, to compare with their statistics we need to know the source galaxy number density as a function of surface brightness. Fontana et al. (2000) do not give surface brightnesses for the galaxies in their Hubble Deep Field catalog, but they do provide magnitudes and half-light radii for galaxies observed in the NTT Deep Field. From their catalog, we derive number densities of galaxies with $\mu_R < 24 \text{ mag arcsec}^{-2}$ of 6.9, 1.7, and 9.0 arcmin^{-2} for our three source redshift bins. Fontana et al. do not give estimates for their incompleteness at these surface brightnesses. From figure 10, we can see that GIF simulation lenses at $z > 0.6$ primarily produce arcs from sources at $z_s \gtrsim 2$, so for simplicity we will only count these sources in our statistics.

From the GIF simulation outputs at $z = 0.62$ and $z = 0.82$, we would expect ~ 1 arc in the RCS field with length-to-width ratios exceeding 10, and distances from the cluster center exceeding $10''$. Gladders et al. find four such arcs around three clusters in their primary sample. In addition, they also report another giant arc at smaller radii. Dropping the cut on $d \geq 10''$ increases the expected number of arcs with length-to-width ratio $r \geq 10$ to ~ 2 , while painting galaxies with $\sigma = 350 \text{ km/s}$ onto the clusters increases the expected number of arcs to ~ 5 .

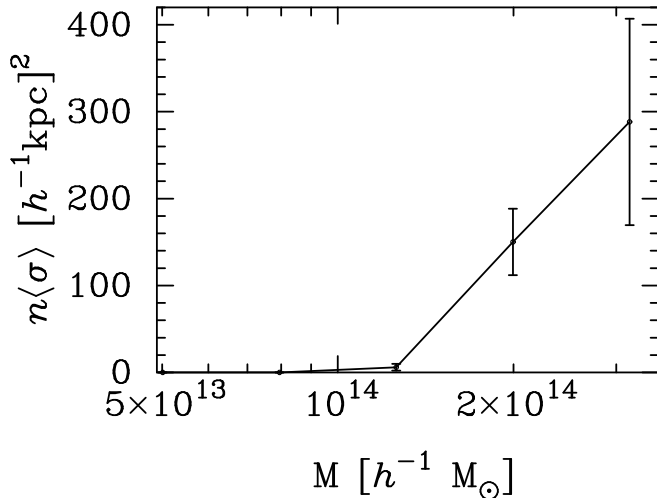


FIG. 11.— Number weighted cross-section at redshift $z = 0.82$ for sources at $z_s = 2$. The strong rise out to the largest masses may indicate that the dominant lenses are not represented in the GIF volume at high redshifts.

In addition to the arc candidates included in their primary sample, Gladders et al. (2003) also report the discovery of three arc-producing clusters found in a follow-up survey of clusters with redshifts $z > 0.95$. Two of the clusters have arcs at small radii, however the third, RCS 2319.9+0038, has multiple arcs at $\gtrsim 10''$.

The RCS statistics may indicate an excess of giant arcs observed at high redshifts, in contrast to the low-redshift agreement found between EMSS and the expected GIF arc statistics. The excess appears to be due to the presence of extremely massive and/or concentrated clusters in the RCS fields which are not present in the GIF volume. For example, RCS 2319.9+0038 has $\approx 10^{14.2} h^{-1} M_\odot$ enclosed within the central $20''$, while the most massive cluster in the $z = 1$ GIF volume has less than twice that mass inside its virial radius! The high fraction of multiple-arc systems in the RCS sample further supports the notion argued by Gladders et al. that a few “super-lenses” are responsible for much of the optical depth, although a full treatment of multiple arc systems must take into consideration source clustering, which is certainly important in at least some multi-arc clusters (e.g Sand et al. 2002).

Unfortunately, these rare clusters are precisely the clusters for which the small volume ($\sim 10^6 h^{-3} \text{Mpc}^3$) we use is deficient in describing the much larger volume ($> 10^8 h^{-3} \text{Mpc}^3$ comoving) probed by the RCS sample. Massive objects like RCS 2319.9+0038, which evidently occur only once or so per RCS volume, will almost certainly never appear in a volume two orders of magnitude smaller. Indeed, examination of the giant arc optical depth as a function of mass at the relevant redshifts (Figure 11) indicates that we are missing the objects which dominate the optical depth. Accordingly, we cannot say at present whether the RCS results are consistent or not with the Λ CDM model.

4. COMPARISON WITH PREVIOUS WORK

We find rough agreement with the optical depths reported by B98 for giant arcs with length-to-width ratios

$r \geq 10$. Nevertheless, we do not find that this optical depth leads to an order of magnitude deficit in the number of arcs expected in EMSS clusters compared to the observed number. Part of the difference between our conclusions and those of B98 stems from the difference in estimates for cluster number counts. We have estimated this using directly the EMSS sky coverage reported in Henry et al. (1992), while B98 assume a number density for EMSS clusters corresponding to about twice the sky density we have estimated. In addition, B98’s estimate for the source density is lower than our estimate (based on counts from the Hubble Deep Fields) also by a factor of two. This combined with our somewhat larger optical depths accounts for the difference in our conclusions. One puzzling difference between our results is that B98 find a much steeper dependence of optical depth on arc length-to-width ratio. We have quoted statistics for arcs with $r \geq 10$. For lower thresholds, e.g. $r \geq 7.5$, our optical depths increase by a factor ~ 2 . In contrast, B98 find that the optical depth for $r \geq 7.5$ is nearly an order of magnitude larger than that for length-to-width ratio of 10. Theoretically, one might expect the cross section to scale like $\sigma \propto l_c \delta(\mu)$, where l_c is the caustic length and δ is the distance from the caustic for which sources are magnified by μ . Near folds, the magnification scales like $\mu \propto \delta^{-1/2}$, while near cusps the magnification scales like $\mu \propto \delta^{-1}$ (Schneider et al. 1992). Naively, assuming r is proportional to μ near critical lines, one might expect the cross section to scale like $\sigma \propto 1/r^{1-2}$, consistent with the moderate rise in τ with declining r which we find. We also note that other workers (Oguri et al. 2003; Wambsganss et al. 2003) find r dependence similar to ours in their simulations, and certainly the observed counts of giant arcs do not show such a steep dependence on length-to-width ratio.

We do not reproduce the enhanced optical depths of Wambsganss et al. (2003), and in particular we do not find as steep a redshift dependence. For example, their reported optical depth at $z_s = 1.5$ of $\tau = 2.3 \times 10^{-6}$ is a factor of 3 larger than our value. It is possible that part of this discrepancy could be attributed to their use of arc magnification as a proxy for length-to-width ratio; as shown in figure 2 this could overestimate the cross section by a factor of 2-3.

The weaker dependence on source redshift is more difficult to explain. The main difference between our strategies was that we only included material within ~ 100 Mpc of the cluster and did not integrate along the entire light cone. However, given the expected fluctuations of only $\sim 1\%$ of the critical surface density, it seems unlikely that large scale structure could affect the lensing cross-section significantly. It is possible to significantly enhance the cross-section with small fluctuations in surface density for lenses with Einstein radii much smaller than the scale radius, where the surface density profile is extremely shallow, but this is not the regime in which we expect to see giant cluster arcs. We have explicitly checked that the addition of extra surface density at the level of $\delta\kappa \approx 3\%$ changes the giant arc cross section by $\lesssim 5\%$ for the massive clusters which dominate the optical depth.

The simulations of Wambsganss et al. had significantly higher force resolution than the GIF simulations:

Wambsganss et al. used N-body simulations with ~ 3 kpc force resolution, while the GIF simulations had force resolution of $20 h^{-1}$ kpc. However, $20 h^{-1}$ kpc is still well within the typical radii at which these giant arcs form, and we have argued in §2.2.5 that this resolution is sufficient to calculate the total optical depth to forming giant arcs. At present, we do not have a good understanding for the different behavior with redshift but our investigations of the effects of central galaxies showed that it is possible that the redshift behavior is sensitive to which arcs are considered to be giant cluster arcs.

The enhanced cross-sections found by Oguri et al. (2003) are also puzzling, since the main effect seems to come from considering steeper profiles in the inner region ($\sim 10 - 20$ kpc), well inside typical Einstein radii ($\sim 50 - 100$ kpc). Again, this could plausibly be a sensitivity in the total cross-section to the details of the central region that is in reality not relevant to the problem of giant cluster arcs.

Gladders et al. (2003) have suggested that “super-lenses”, objects with low mass but large cross section, may be responsible for much of the optical depth. Their argument for low masses hinges on the assumption that the cross-section for giant arcs scales linearly with the mass, but fig. 4 shows that a more reasonable estimate is $\sigma \propto M^{3-4}$. With this steeper scaling it is plausible that “superlenses” are primarily simply more massive clusters. Weak lensing mass maps at larger radii or Sunyaev-Zeldovich measurements can answer the question of whether high-redshift lenses like RCS 2319.9+0038 are supermassive (e.g. $M \sim 10^{15} h^{-1} M_{\odot}$) or not. If these objects have lower masses (e.g. $\text{few} \times 10^{14} h^{-1} M_{\odot}$), then their large Einstein radii are puzzling. Meneghetti et al. (2003c) and Torri et al. (2003) have suggested that cluster mergers may account for a significant fraction of the giant arc optical depth. However, note that the critical lines traced out by the multiple-arc systems of Gladders et al. appear relatively round, in contrast to the highly elongated critical lines expected of low mass clusters whose giant arc cross sections have been enhanced by ongoing mergers (Meneghetti et al. 2003c; Torri et al. 2003). Another possibility is that “super-lenses” may be ordinary mass, but super-concentrated. An example of this may be CL0024+1654, for which a recent combined strong- and weak-lensing analysis (Kneib et al. 2003) indicates a concentration $c_{200} \approx 22$. Such high concentrations are extremely anomalous for simulated CDM galaxy clusters (e.g. Bullock et al. 2001). If the RCS super-lenses turn out to have similarly deviant concentrations, and such objects are commonplace, their existence could pose a serious challenge to our understanding of

structure formation in the Λ CDM model.

5. DISCUSSION AND CONCLUSIONS

At present, there appears to be no discrepancy between observed giant arc statistics and predictions from the Λ CDM model at low redshifts $z \lesssim 0.6$. Imaging of EMSS clusters by Le Fevre et al. (1994) and Luppino et al. (1999) indicates that ~ 900 giant arcs are expected over the full sky from X-ray bright clusters at these redshifts, while ray-tracing through clusters taken from the GIF simulations leads us to expect ~ 1000 giant arcs. At higher redshifts $z \gtrsim 0.6$, the observed abundance of close-in arcs with $d \lesssim 10''$ observed by the LCDCS and RCS appears consistent with expectations, when the effects of the central galaxies are included in the gravitational potential. However, there may be an excess of wide separation ($d \gtrsim 10''$) giant arcs at high redshift. This putative excess appears to be due to extremely massive or unusually concentrated clusters not present in the (admittedly limited) simulation volumes we have employed.

Looking forward, upcoming X-ray cluster surveys like MACS (Ebeling et al. 2001) and wide-area surveys like the CFHT Legacy Survey⁴ and the Sloan Digital Sky Survey⁵ can be expected to improve the statistics of giant arcs on the sky. For example, the RCS-2 survey covers an area of 830 deg^2 and is expected to produce $\sim 50 - 100$ new arcs (M. Gladders, private communication). Deep surveys can also begin to test CDM predictions for giant arc properties. As we have discussed earlier, CDM clusters tend to produce arcs along (but aligned orthogonal to) their major axes. This is modified somewhat by the presence of central cD galaxies in the clusters, however for reasonable velocity dispersions we expect the arc angular distribution to be anisotropic. Multi-arc systems may provide a probe of halo triaxiality at small radii, complementary to weak lensing studies at large radii (e.g. Hoekstra et al. 2003).

We thank Paul Bode and Jerry Ostriker for help with N-body simulations and for making publicly available their TreePM code. We also thank Matthias Bartelmann, Mike Gladders and Massimo Meneghetti for helpful discussions. N. D. acknowledges the support of NASA through Hubble Fellowship grant #HST-HF-01148.01-A awarded by the Space Telescope Science Institute, which is operated by the Association of Universities for Research in Astronomy, Inc., for NASA, under contract NAS 5-26555. G.H. is supported by the W. M. Keck Foundation. J. F. H. is supported by a Proctor Fellowship granted by Princeton University.

⁴ <http://www.cfht.hawaii.edu/Science/CFHLS>

⁵ <http://www.sdss.org>

APPENDIX

ON LIPS AND NAKED CUSPS

In section §2.2.4 the addition of a centrally concentrated mass was shown to have a significant effect on where giant arcs can form. We can understand this behavior as follows. On the critical curves, the magnification matrix becomes singular, causing sources to become highly magnified along one direction. The highly elongated direction, however, is not in general parallel to the critical line itself. In some instances, the magnified direction can be perpendicular to the critical line, i.e. it can point along $\nabla\mu$. Such cases clearly are not conducive to the formation of giant arcs, as the magnification diminishes so quickly along their lengths that these arcs are unable to acquire ‘giant’ dimensions.

Instead, giant arcs form preferentially at locations where the magnified direction is aligned with the tangent to the critical curve.

The direction along which arcs are elongated is determined by the orientation of the local shear. For our purposes, the shear has two principal sources: the tidal gravity associated with the radial density gradient, and the triaxiality and substructure of the dark matter distribution. The former produces shear which is azimuthally oriented with respect to the central mass concentration, while the latter lead to shear aligned with the principal axes of the density distribution. The competition between these two effects determines whether arcs are primarily tangential or ‘Cartesian’, which determines whether the caustic structure is that of lips, or radial and tangential caustics.

N-body simulations in the cold dark matter model tend to produce clusters which have shallow radial profiles and strong triaxiality. Average radial profiles exhibit r^{-1} density cusps (e.g Navarro et al. 1997) which, in projection, give surface densities rising only logarithmically at small radii. Typical clusters are also quite triaxial, with axis ratios on average near 0.5 with large scatter (e.g Jing & Suto 2002; Thomas et al. 1998). Because of this, a large fraction of GIF clusters have lips caustics, although this depends in part on projection. Clusters viewed along their major axes have larger central surface densities and less ellipticity than other projections, meaning that clusters can have radial and tangential caustics viewed along certain projections, and lips when viewed in other orientations.

In figure A12 we plot the caustics and critical lines for an elliptical NFW profile, and lensed images of representative sources. The top panel illustrates typical caustic patterns for the pure DM simulations. There are two critical lines, pointing along and orthogonal to the cluster major axis. However, as the lensed arcs indicate, the magnified direction along the outer critical line tends to point up and down. Because of this, the corresponding caustics in the source plane take the form of lips catastrophes, with two cusps each, corresponding to the two locations on each critical line where the highly magnified direction becomes tangent to the curve (Schneider et al. 1992). This is why long, thin arcs preferentially form at the ends of the critical lines in this case.

The caustic structure changes as the central mass concentration increases, shown in the bottom two panels of the figure. As the central mass is increased, the tangential shear grows commensurate to the ellipticity-induced shear, and the two critical lines approach each other. When they meet, their corresponding caustics meet at a hyperbolic umbilic catastrophe (Schneider et al. 1992), shown in the middle panel of figure A12. Near hyperbolic umbilics, the source becomes highly magnified in *both* directions, which again is not favorable for producing long, thin arcs. For higher central concentrations, the critical curves become tangential and radial; that is, their magnified directions tend to point in the azimuthal and radial directions, for the outer and inner curves, respectively. The near alignment of the magnified direction with the curve tangent, for the tangential critical line, allows long thin arcs to form all along its length, as depicted in the bottom panel of figure A12.

REFERENCES

- Bahcall, N. & Fan, X. 1998, *ApJ*, 504, 1
- Bartelmann, M., Huss, A., Colberg, J. M., Jenkins, A., & Pearce, F. R. 1998, *A&A*, 330, 1
- Bartelmann, M., Meneghetti, M., Perrotta, F., Baccigalupi, C., & Moscardini, L. 2003, *A&A*, in press, astro-ph/0210066
- Bartelmann, M. & Weiss, A. 1994, *A&A*, 287, 1
- Blain, A. W., Kneib, J.-P., Ivison, R. J., & Smail, I. 1999, *ApJ*, 512, L87
- Bullock, J. S., Kolatt, T. S., Sigad, Y., Somerville, R. S., Kravtsov, A. V., Klypin, A. A., Primack, J. R., & Dekel, A. 2001, *MNRAS*, 321, 559
- Ebeling, H., Edge, A. C., & Henry, J. P. 2001, *ApJ*, 553, 668
- Flores, R. A., Maller, A. H., & Primack, J. R. 2000, *ApJ*, 535, 555
- Fontana, A., D’Odorico, S., Poli, F., Giallongo, E., Arnouts, S., Cristiani, S., Moorwood, A., & Saracco, P. 2000, *AJ*, 120, 2206
- Gladders, M. D., Hoekstra, H., Yee, H. K. C., Hall, P. B., & Barrientos, L. F. 2003, *ApJ*, 593, 48
- Gladders, M. D., Yee, H. K. C., & Ellingson, E. 2002, *AJ*, 123, 1
- Haiman, Z., Mohr, J. J., & Holder, G. P. 2001, *ApJ*, 553, 545
- Henry, J. P., Gioia, I. M., Maccacaro, T., Morris, S. L., Stocke, J. T., & Wolter, A. 1992, *ApJ*, 386, 408
- Hoekstra, H., Yee, H. K. C., & Gladders, M. D. 2003, *ArXiv Astrophysics e-prints*, astro-ph/0306515
- Jing, Y. P. & Suto, Y. 2002, *ApJ*, 574, 538
- Kauffmann, G., Colberg, J. M., Diaferio, A., & White, S. D. M. 1999, *MNRAS*, 303, 188
- Keeton, C. R. 2001, *ArXiv Astrophysics e-prints*, astro-ph/0102340
- Kneib, J., Hudelot, P., Ellis, R. S., Treu, T., Smith, G. P., Marshall, P., Czoske, O., Smail, I., & Natarajan, P. 2003, *ApJ*, in press, astro-ph/0307299
- Le Fevre, O., Hammer, F., Angonin, M. C., Gioia, I. M., & Luppino, G. A. 1994, *ApJ*, 422, L5
- Luppino, G. A., Gioia, I. M., Hammer, F., Le Fèvre, O., & Annis, J. A. 1999, *A&AS*, 136, 117
- Meneghetti, M., Bartelmann, M., & Moscardini, L. 2003a, *ArXiv Astrophysics e-prints*, astro-ph/0302603
- . 2003b, *MNRAS*, 340, 105
- Meneghetti, M., Bartelmann, M., Moscardini, L., Rasia, E., Tormen, G., & Torri, E. 2003c, *ArXiv Astrophysics e-prints*, astro-ph/0305047
- Meneghetti, M., Bolzonella, M., Bartelmann, M., Moscardini, L., & Tormen, G. 2000, *MNRAS*, 314, 338
- Meneghetti, M., Yoshida, N., Bartelmann, M., Moscardini, L., Springel, V., Tormen, G., & White, S. D. M. 2001, *MNRAS*, 325, 435
- Metcalfe, L., Kneib, J.-P., McBreen, B., Altieri, B., Biviano, A., Delaney, M., Elbaz, D., Kessler, M. F., Leech, K., Okumura, K., Ott, S., Perez-Martinez, R., Sanchez-Fernandez, C., & Schulz, B. 2003, *A&A*, 407, 791
- Navarro, J. F., Frenk, C. S., & White, S. D. M. 1997, *ApJ*, 490, 493
- Oguri, M., Lee, J., & Suto, Y. 2003, *ApJ*, submitted, astro-ph/0306102
- Power, C., Navarro, J. F., Jenkins, A., Frenk, C. S., White, S. D. M., Springel, V., Stadel, J., & Quinn, T. 2003, *MNRAS*, 338, 14
- Sand, D. J., Treu, T., & Ellis, R. S. 2002, *ApJ*, 574, L129
- Schneider, P., Ehlers, J., & Falco, E. E. 1992, *Gravitational Lenses* (Gravitational Lenses, XIV, 560 pp. 112 figs.. Springer-Verlag Berlin Heidelberg New York. Also Astronomy and Astrophysics Library)
- Smail, I., Ivison, R. J., Blain, A. W., & Kneib, J.-P. 2002, *MNRAS*, 331, 495
- Spergel, D. N., Verde, L., Peiris, H. V., Komatsu, E., Nolte, M. R., Bennett, C. L., Halpern, M., Hinshaw, G., Jarosik, N., Kogut, A., Limon, M., Meyer, S. S., Page, L., Tucker, G. S., Weiland, J. L., Wollack, E., & Wright, E. L. 2003, *ApJS*, 148, 175
- Thomas, P. A., Colberg, J. M., Couchman, H. M. P., Efsthathiou, G. P., Frenk, C. S., Jenkins, A. R., Nelson, A. H., Hutchings, R. M., Peacock, J. A., Pearce, F. R., & White, S. D. M. 1998, *MNRAS*, 296, 1061
- Torri, E., Meneghetti, M., Bartelmann, M., Moscardini, L., Rasia, E., & Tormen, G. 2003, in preparation

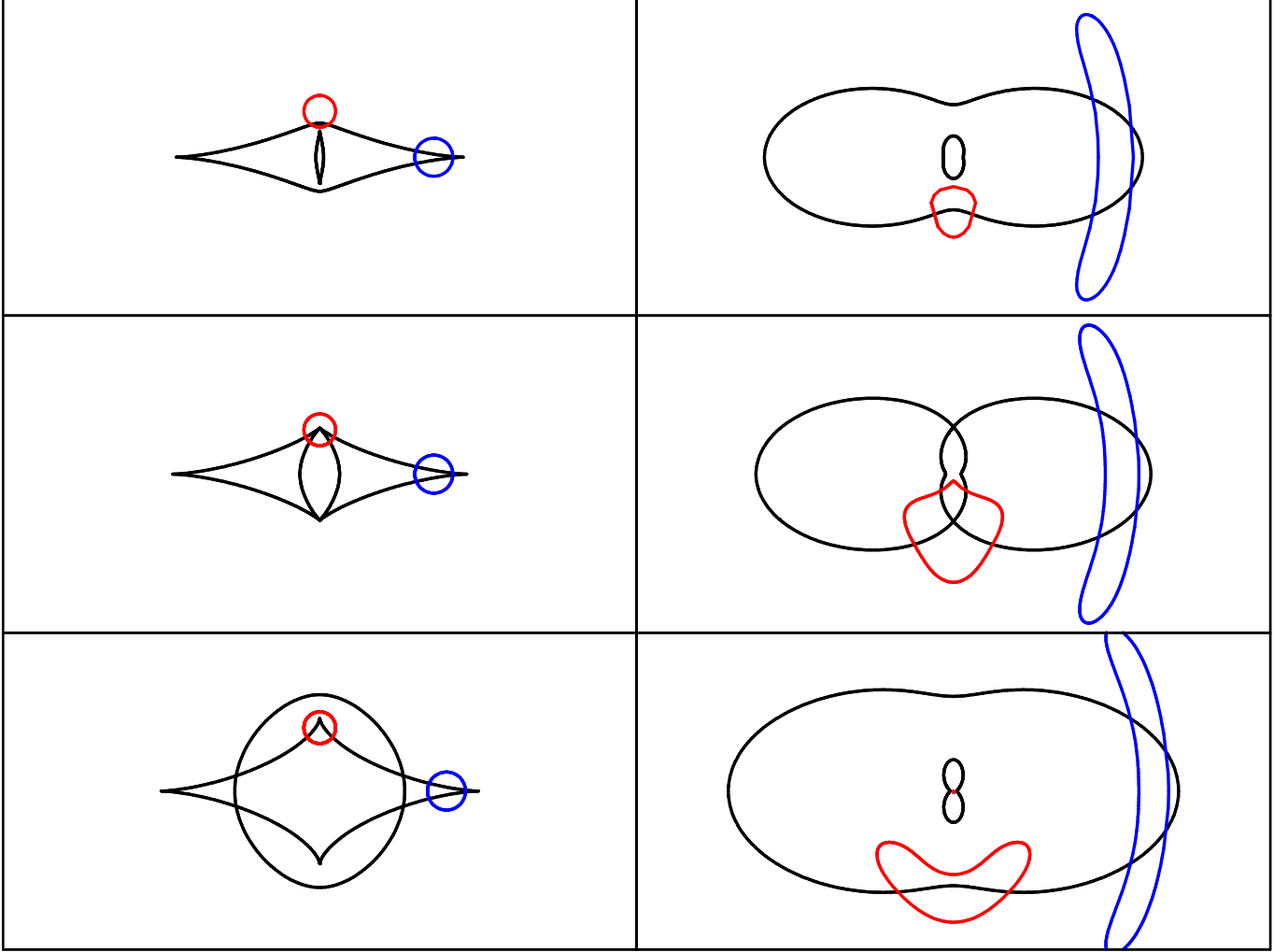


FIG. A12.— Critical lines and caustic structure as a function of central mass concentration. The top panel depicts lensing by an elliptical NFW profile, while the bottom two panels show the effect of adding increasingly massive central galaxies, modeled as Jaffe profiles. Critical lines, caustics, and arcs were computed in this figure using the software of Keeton (2001).

Wambsganss, J., Bode, P., & Ostriker, J. P. 2003, ApJ, submitted, astro-ph/0306088

Williams, L. L. R. & Lewis, G. F. 1998, MNRAS, 294, 299

Williams, L. L. R., Navarro, J. F., & Bartelmann, M. 1999, ApJ, 527, 535

Zaritsky, D. & Gonzalez, A. H. 2003, ApJ, 584, 691